A multi-stack simulation of shunt currents in vanadium redox flow batteries

F.T. Wandschneider [a,*], S. Röhm [a], P. Fischer [a], K. Pinkwart [a], J. Tübke [a], H. Nirschl [b]

[a] Fraunhofer-Institute for Chemical Technology, Department of Applied Electrochemistry, Joseph-von-Fraunhofer-Strasse 7, D-76327 Pfinztal, Germany
[b] Karlsruhe Institute for Technology, Institute for Mechanical Process Engineering and Mechanics, Strasse am Forum 8, D-76131 Karlsruhe, Germany

HIGHLIGHTS

- A model of the shunt currents in several stacks is developed.
- The model allows for state-of-charge dependent electrolyte conductivities.
- External shunt currents between stacks affect the shunt currents within stacks.

ARTICLE INFO

ABSTRACT

A model for the shunt currents in an all-vanadium redox flow battery consisting of 3 stacks which are electrically connected in series. It is based on an equivalent circuit which treats the shunt current pathways as Ohmic resistors. The conductivity of the vanadium electrolyte has been measured for different state-of-charges in order to implement a dependency of the resistances on the state-of-charge of the system. Published results are used to validate the simulation data of a single stack.

Three setups of pipe networks are evaluated using the model. The pipe connections between the stacks give rise to external shunt currents, which also increase the amount of shunt currents within the stacks. These connections also lead to a nonuniform distribution of the shunt currents. The effects of the shunt currents on the Coulombic efficiency and the energy efficiency of the system are studied by the means of the model.

1. Introduction

Redox flow batteries are electrochemical energy storage devices that combine qualities of batteries and fuel cells [1]. The storage medium is an electrolyte solution which, for most redox flow battery types, does not undergo a phase change during the electrochemical reaction. The reaction takes place in stacks of cells whereas the main part of the electrolyte solution is stored in external tanks; the electrolyte solution is constantly pumped in a closed loop between the tanks and the stack. Storage capacity and power conversion can thus be designed separately [2]. This battery type is, amongst others, suitable for large-scale applications like temporary storage of electrical energy generated from wind or photovoltaic farms [3–6]. The focus of this work is the all-vanadium redox flow battery type which was pioneered by Skyllas-Kazacos et al. [7].

Both the feed and removal of electrolyte solution to and from the stacks and the individual cells is implemented using shared pipe works. This creates two additional ionic connections between the cells and stacks in addition to the electrical connections via the bipolar plates. During charge and discharge of the battery additional currents, called leakage currents or shunt currents, will form along the ionic connections. The shunt current pathways in a redox flow battery with two cells are depicted in Fig. 1.

The occurrence of shunt currents is also reported in bipolar electrolyzers [8,9] and liquid fuel cells [10]. For redox flow batteries, shunt currents were originally investigated by NASA [11–13]. The models to evaluate the magnitude and effects of the shunt currents combine two sets of properties. These are the properties of the redox flow battery stack and the transient properties for charge and discharge operations. These are incorporated into an equivalent

* Corresponding author.
  E-mail addresses: frank.wandschneider@ict.fraunhofer.de, frank.wandschneider@gmx.de (F.T. Wandschneider).
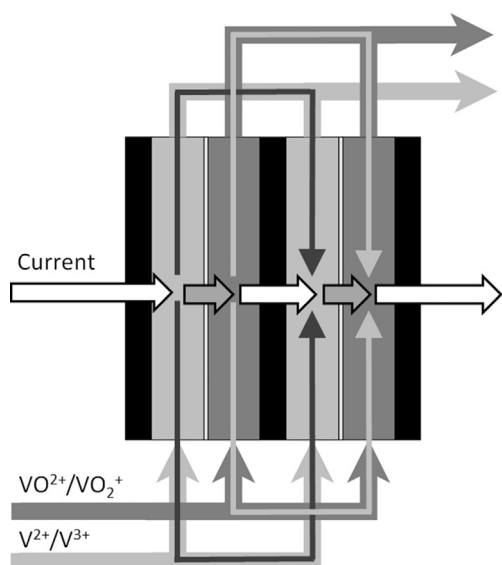 URL: http://www.ict.fraunhofer.de/de/komp/ae/rfb.html

Fig. 1. Electric and ionic currents in a vanadium redox flow battery with two cells.

circuit of the stack and sets of differential equations are then generated. An equivalent circuit for a redox flow battery is shown in Fig. 2; the resistor designations are explained in Section 3.1.

The charge and discharge properties can be static to allow an analytical approach in solving for the effects of single parameters or sets of parameters [11,14]. More common is a numerical approach in solving the equations of the model [15–19,10,20] for a combination of static battery properties and time-dependent charge and discharge operation properties. Codina and Aldaz [15] used their model to evaluate the effects of shunt currents between three stacks of an iron chromium redox flow battery. Tang et al. [21] have proposed a fully dynamic model for both the properties of battery operation and properties of the electrolyte solutions of the vanadium redox flow battery. For the latter, they introduce the effects of vanadium crossover, i.e. the diffusion of vanadium ions across the separating membrane and the ensuring side reactions [22].

This work is part of preliminary studies for the construction of a vanadium redox flow battery to buffer the electricity generated by a 2 MW wind turbine at the site of the Fraunhofer Institute for Chemical Technology. The battery specification calls for a peak power performance of 2 MW and a storage capacity of 20 MWh. At least 600 m^3 of a 1.6 M vanadium electrolyte solution will be needed to realize this capacity. Computer aided process engineering (CAPE) is used in order to speed up the development process of

the vanadium redox flow battery system and its electrical connection to the wind turbine [23]. CAPE will also be used to optimize the operating parameters, this is important to make the battery economically viable [24].

The aim of this work is to develop a first model for shunt currents which occur in sets of vanadium redox flow battery stacks that are electrically connected in series and share a common electrolyte feed and removal pipe network. The electric series connection is needed to realize the operational voltage of the rectifiers and the inverters of a large redox flow battery installation. Shunt currents between the stacks could be avoided by providing a separate pipe network for each stack; however, this increases the needed pumping power and decreases the overall energy efficiency [25]. The proposed model in this report also features dynamic properties for both anolyte and catholyte solutions depending on the state-of-charge of the system.

2. Experimental details

The starting electrolyte for both vanadium half-cells was an aqueous solution of 0.8 mol l^{-1} vanadyl sulphate $VOSO_4$, 0.4 mol l^{-1} di-vanadium tri-sulphate $V_2(SO_4)_3$, 2 mol l^{-1} sulfuric acid H_2SO_4 and 0.05 mol l^{-1} phosphoric acid H_3PO_4 were used (GfE Metalle und Materialien GmbH, Germany). A vanadium redox flow battery with an anion exchange membrane (FAP-0, FumaTech GmbH, Germany) was used to prepare the anolyte and catholyte solutions. The starting electrolyte underwent electrodialysis at a current density of 25 mA cm^{-2}. Several anolyte and catholyte solutions corresponding to a state-of-charge of zero respective one were prepared. These were used to produce mixtures of electrolyte solutions to adjust for different state-of-charges for each half-cell. The state-of-charge of the resulting solutions was measured by cerimetric titration. The conductivity of these electrolyte solutions was then measured with a conducting meter (SevenEasy Conductometer, Mettler-Toledo Inc., Switzerland). The conductivity measurements were done with fresh solutions at different temperatures (GD 120 Thermostat, Grant Instruments Ltd., United Kingdom) between 20 °C and 35 °C.

3. Model assumptions and equations

3.1. Analog circuit method

The stack is described as a network of electrical elements, shown in Fig. 2 for a single stack. The network is made up from resistors for the internal cell resistances and the shunt current path resistances, voltage sources for cell potentials and a current source that provides
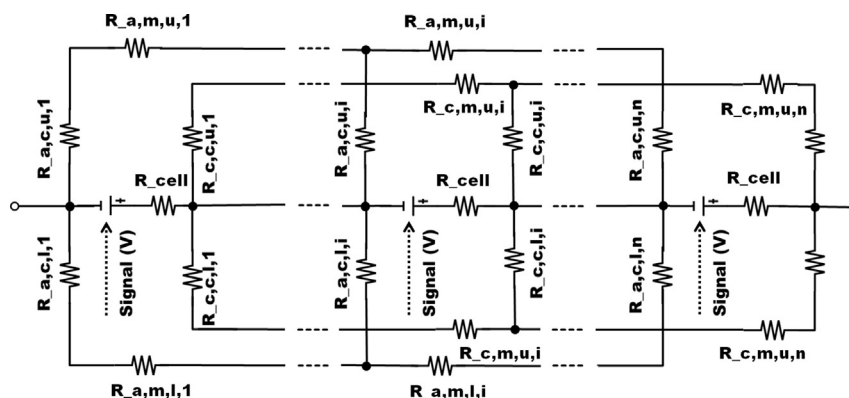

Fig. 2. Equivalent circuit diagram of the internal shunt currents within a redox flow battery stack consisting of *n* individual cells.

the constant charge respective discharge current. Current balances can be setup by applying Kirchhoff's law to each cell. The formulation of these balances, the resulting sets of linear equations and one approach of solving them can be found in Ref. [14].

Many equivalent electrical elements are needed to fully describe a large redox flow battery stack. Therefore, a naming scheme is introduced. The resistors are designated R and the underline character indicates the following characters as subscript. The first character indicates anolyte (a) or catholyte (c), the second the geometry part (c − channel or m − manifold), the third the location relative to the cell (l - lower respective feed flow or u − upper respective removal flow) and the last character is the number of the cell.

Two possible battery systems of three stacks and the pipe network connection between them are presented in Fig. 3. Their equivalent circuits are shown in Figs. 4 and 5. In these cases, the second character of the subscript of a resistor variable can also be p − pipe or t − tube.
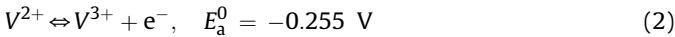
3.2. Electrochemical model

The model assumes a uniform distribution of the fluid flow within the stack and the performance equality of all cells.

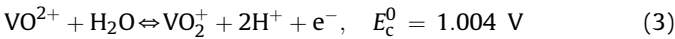The voltage of a single cell E_{cell} is calculated as

$$E_{cell} = E_{Nernst} + \eta_{act}. \tag{1}$$

E_{Nernst} is the cell potential depending on the ion concentrations and η_{act} the activation overpotential needed to trigger the electrochemical reaction.

The potential of the cells changes depending on the reactions in the anode half-cell

$$V^{2+} \Leftrightarrow V^{3+} + e^-, \quad E_a^0 = -0.255 \ V \tag{2}$$

and the cathode half-cell

$$VO^{2+} + H_2O \Leftrightarrow VO_2^+ + 2H^+ + e^-, \quad E_c^0 = 1.004 \ V \tag{3}$$

leading to the total cell reaction

$$V^{2+} + VO_2^+ + 2H^+ \Leftrightarrow V^{3+} + VO^{2+} + H_2O, \quad E_{cell}^{00} = 1.259 \ V. \tag{4}$$
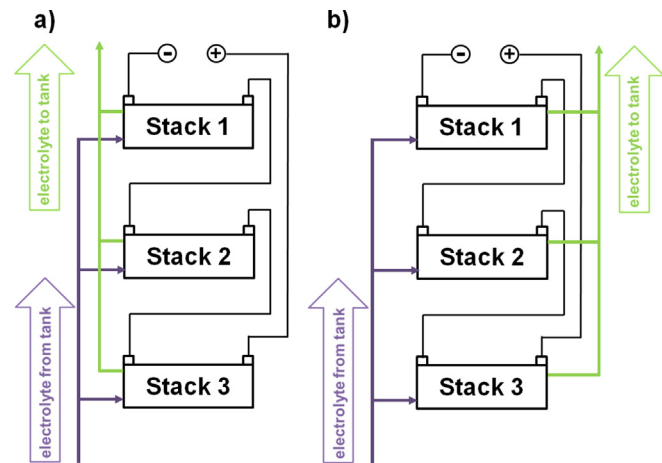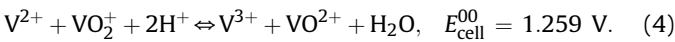

Fig. 3. Three vanadium redox flow battery stacks electrically connected in series. The inlet and outlet for the electrolyte solutions are either a) on the same side or b) on opposite sides. In this figure, only the anolyte is depicted; the inlet and outlet of the catholyte is ordered in the same way.

E^0 is the standard half-cell reduction potential; the subscript indicates anode or cathode. The cell potential E can be calculated with the standard cell potential E_{cell}^{00} by the Nernst equation

$$E_{Nernst} = E_{tot}^{00} + \frac{\mathbf{R}T}{\mathbf{F}} \ln \frac{a(V^{2+})a\left(VO_2^+\right)a^2(H^+)}{a(V^{3+})a(VO^{2+})a(H_2O)}. \tag{5}$$

$\mathbf{R}$ is the universal gas constant, T the cell temperature, $\mathbf{F}$ the Faraday constant and the activity of the ionic species. Assuming the activity of the protons and the water molecules and the activity coefficients of the vanadium species to be unity, the equation becomes

$$E_{Nernst} = E_{tot}^{00} + \frac{\mathbf{R}T}{\mathbf{F}} \ln \frac{c(V^{2+})c\left(VO_2^+\right)}{c(V^{3+})c(VO^{2+})}. \tag{6}$$

Further assuming that there is no diffusion of vanadium ions across the membrane, that there are no side reactions and that the electrolyte volume in both half-cell is constant, the logarithmic argument in Equation (6) can be multiplied by

$$\frac{c(V^{2+}) + c(V^{3+})}{c(V^{2+}) + c(V^{3+})} \frac{c(VO^{2+}) + c\left(VO_2^+\right)}{c(VO^{2+}) + c\left(VO_2^+\right)},$$

yielding

$$E_{Nernst} = E_{tot}^{00} + \frac{2\mathbf{R}T}{\mathbf{F}} \ln \frac{SOC}{1 - SOC}. \tag{7}$$

The state-of-charge SOC is defined as

$$SOC = \frac{c(V^{2+})}{c(V^{2+}) + c(V^{3+})} = \frac{c\left(VO_2^+\right)}{c(VO^{2+}) + c\left(VO_2^+\right)}. \tag{8}$$

For the activation potential, only Ohmic losses are considered, yielding

$$\eta_{act} = I_{cell} \ R_{cell}. \tag{9}$$

I_{cell} is the current passing through a cell and R_{cell} the internal cell resistance.

3.3. Implementation of time-dependency

For a galvanostatic charge or discharge regime of a single cell, a linear correlation between the state-of-charge and time can be assumed [26]. However, the part of the current that bypasses the cells as shunt currents does not take part in the electrochemical conversion within the passed-over cells. In order to account for the actual number of electrochemically converted ions, the molar balance for an ionic species i is

$$\frac{\partial n_{i,t}}{\partial t} = \dot{n}_{i,out} - \dot{n}_{i,in} \equiv \Delta \dot{n}_i. \tag{10}$$

$n_{i,t}$ is the number of moles of species i in the tank, $\dot{n}_{i,out}$ the molar flux coming back from the cells and $\dot{n}_{i,in}$ the molar flux to the cells. Assuming the pipe volume negligible against the volume of the tank and again, that there are no side reactions, the molar change of the species i $\Delta \dot{n}_i$ depends on the electrochemical conversion in the cells of the stack(s). Applying the first Faraday law for a given time step Δt, this is expressed as

$$\Delta \dot{n}_i = \int \frac{\sum^{stacks} \sum^{cells} I_{cell}}{\mathbf{F} \Delta t} \ dt. \tag{11}$$
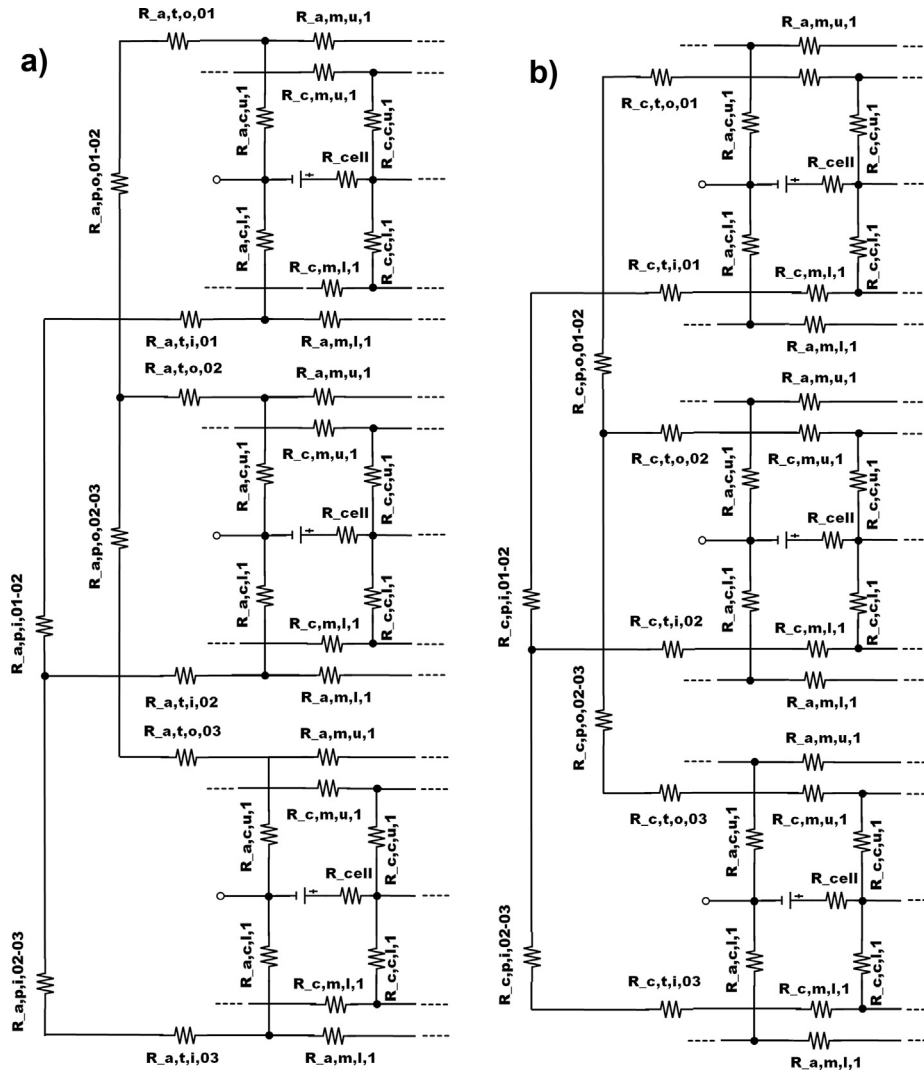
Fig. 4. Equivalent circuit diagram of the external shunt currents between three redox flow battery stacks with inlets and outlets on the same side. In the subfigures, the anolyte (a) and catholyte (b) pathways are shown.

The inner term in the enumerator is the sum of the currents passing the resistors that represent the inner resistances of the cells. Without side reactions, this quotient equals the number of converted moles. As the volume of pipes and cells is neglected, Equation (8) becomes

$$S = \frac{c(V^{2+})V_t}{(c(V^{2+}) + c(V^{3+}))V_t} = \frac{n_{V^{2+}}}{n_{tot}} = \frac{n_{VO_2^+}}{n_{tot}}. \tag{12}$$

S is the time-dependent state-of-charge, V_t the volume of the tank and n_{tot} is the total number of all vanadium ions in the anolyte or catholyte.

3.4. State-of-charge dependent conductivity

The conductivities of Vanadium anolyte (V^{2+}/V^{3+}) and catholyte ($V(IV)O^{2+}/V(V)O_2^+$) solutions were measured for different state-of-charges at different temperatures. The values for the state-of-charges of 0 and 1 are shown in Table 1. The conductivity of an electrolyte for a given time is calculated by the linear approximations

$$\lambda_a(t) = \sigma_{V(III)} + S\left(\sigma_{V(II)} - \sigma_{V(III)}\right), \tag{13}$$

$$\lambda_c(t) = \sigma_{V(IV)} + S\left(\sigma_{V(V)} - \sigma_{V(IV)}\right). \tag{14}$$

λ_a and λ_c are the anolyte and catholyte conductivities; $\sigma_{V(II)}$, $\sigma_{V(III)}$, $\sigma_{V(IV)}$ and $\sigma_{V(V)}$ are the specific conductivities of the electrolytes containing the ions of a single vanadium species. Their respective values are taken from Table 1; the temperature within the model is assumed to be 293 K. The time-dependent ionic resistance of a fluid part is then calculated as

$$R_{i,j}(t) = \frac{l_j}{\lambda_i(t)A_j}. \tag{15}$$

i denotes anolyte or catholyte and j indicates channel or manifold within the stack or pipe or tube outside of the stack. A is the cross-sectional area within the part and l the length of the part. The quotient l_j/A_j can also be expressed as the ratio of length to diameter for round pipes.
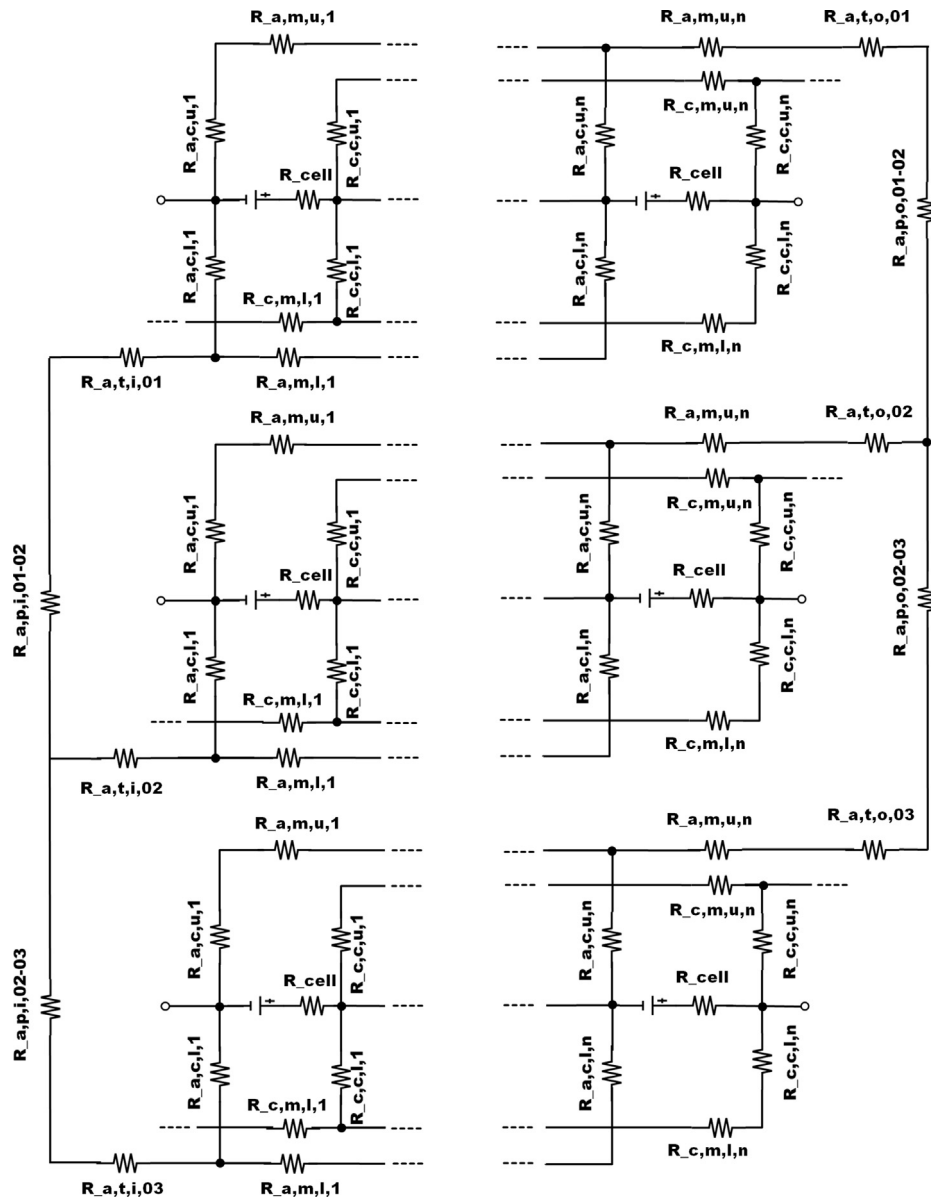
Fig. 5. Equivalent circuit diagram of the external shunt currents between three redox flow battery stacks with inlets and outlets on opposite sides. In this figure, only the external anolyte pathway is shown, the catholyte one is constructed in an analogous manner.

3.5. Numerical details

The model has been implemented and evaluated using Open-Modelica 1.9 Revision 17628 from the Open Source Modelica Consortium. A time step of one second has been used for discretization.

4. Results and discussion

4.1. Conductivity measurements

The conductivities of Vanadium anolyte (V^{2+}/V^{3+}) and catholyte ($V(IV)O^{2+}/V(V)O_2^+$) solutions were measured for different state-of-charges at different temperatures. The values for the state-of-charges of 0 and 1 are shown in Table 1. Comparing our results for a solution of 1.6 M Vanadium and 2 M sulfuric acid to the results of [27] for a solution of 1.5 M Vanadium and 2 M sulfuric acid, our values deviate 6%, −17%, 20% and 7% from the reported values reported for the V(II), V(III), V(IV) and V(V) species respectively. In

Ref. [27] a redox flow battery cell with a cation exchange membrane, which allows the transport of H^+ ions was used. Our cell had an anion exchange membrane, which is permeable for HSO_4^- and SO_4^{2-} ions. The concentration of these ions has a strong influence on the conductivity of the electrolyte solutions [28,27]. The measured conductivities therefore exhibit the same order of magnitude because the initial electrolyte solutions in both cases are similar but the charged solutions vary because of the different cell setups.

4.2. Model validation

In this setup, the model features one single stack of 10 cells. The values for cell resistances, cell voltages and boundary conditions are taken from Ref. [20]. All resistors have constant values. The simulated data from the model are then compared to the experimental and simulated data from this reference. There is good agreement between the measured and calculated data, as shown in Fig. 6. Our calculated data show the very same progression of the

Table 1
Conductivity of vanadium electrolyte solutions at different temperatures. The solutions were prepared using a single-cell redox flow battery with an anion exchange membrane.

Vanadium species	Temperature	Conductivity
	T [K] $\pm$ 0.5 K	σ [mS cm^{-1}] $\pm$ 10 mS cm^{-1}
V(II)	293	275
	298	303
	303	330
	308	358
V(III)	293	175
	298	196
	303	217
	308	238
V(IV)	293	275
	298	308
	303	336
	308	370
V(V)	293	413
	298	454
	303	492
	308	530

Fig. 7. Comparison of simulated (own and [20]) data for the shunt currents in the anolyte manifold and channel at a current density of 60 [mA cm^{-2}] and a state-of-charge of 0.5. Manifold values are presented with solid lines and solid symbols; channel values with dotted lines and outlined symbols; charge cycle black (own) and red [20], discharge cycle magenta (own) and blue [20]. (For interpretation of the references to colour in this figure legend, the reader is referred to the web version of this article.)

function as theirs. The results from both simulations for the anolyte manifolds and channels are compared in Fig. 7. Their simulated data and ours are nearly identical which indicates good agreement of the model to their experiment.

4.3. Expanded model

The size of one single stack is increased to 30 cells, which are based on the design specifications of the planned 9 kW vanadium redox flow battery stack. The specifications are presented in Table 2. The complete battery system in this study comprises three stacks. There is a serial connection between the stacks for the electric current. The last cell of the first stack is connected to the first cell of the second stack and the last cell of the second stack is connected to the first cell of the third stack.

The values for cell resistances, cell voltages and boundary conditions are taken from our experimental stack setup which are shown in Table 2. The resistors representing the resistances of the electrolyte solutions in the channels, manifolds, pipes and tubes are set to dynamic, state-of-charge dependent values. The length of the tubes and pipes has been arbitrarily chosen to low values, like 3 stacks being spaced 50 cm apart and connected by the minimal piping needed. Usually, there are long pipes used between stacks in
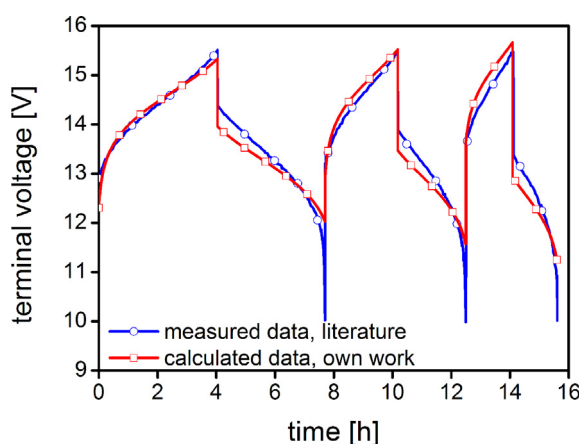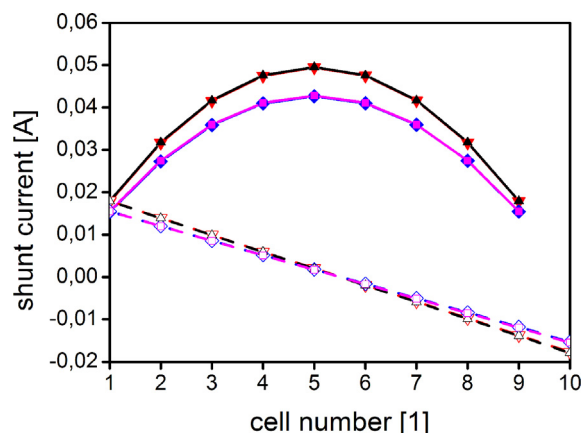
redox flow battery installations with multiple stacks to reduce possible shunt currents. In this work, the short pipe lengths are chosen in order to investigate whether these precautions are needed (Table 3).

In the first case, there is no fluidic connection between the stacks. Fluidic connections then are added to the stacks. The electrolyte fluid flows into and out of the stack are on the same side in the second case which is shown in Fig. 3a). In a third case, the electrolyte fluids enter the stack on one side and leave on the opposite side. Both the inlets and outlets share the same side in this setup. This is depicted in Fig. 3b). The three battery setups are subject to three consecutive galvanostatic charge and discharge cycles at current densities of 25, 50 and 75 mA cm^{-2}. The initial state-of-charge of the electrolyte is 0.05. Each charge operation is conducted until a state-of-charge of 0.95 is reached. The following discharge operation stops at a state-of-charge of 0.05.

The simulated voltage of the three setups for the consecutive galvanostatic charge and discharge cycles are shown in Fig. 8. The charge cycles of the setups with outer connections take longer than in the case without connections. The outer electrolyte connections give rise to shunt currents between the stacks, which diminish the electric current passing through the cells and decreases the cell power. Therefore, it takes longer to convert enough ions to meet the stop criterion of the upper state-of-charge. During the discharge of the battery system, the shunt currents occur in addition to the outer electric current. There is increased electrochemical conversion in the cells to sustain both these currents which leads to a faster depletion of the charged species. The battery system setups with electrolyte connections therefore reach the lower state-of-charge boundary faster than the setup without connections. The longer

Fig. 6. Comparison of measured [20] and simulated data for three charge and discharge cycles of 40, 60 and 80 [mA cm^{-2}].

Table 2
Properties of the vanadium redox flow battery stack.

Property	Value
Dimension of each half-cell [cm^3]	44 $\times$ 82 $\times$ 0.6
Cell resistivity [Ω cm^2]	3.114
Membrane area [cm^2]	3608
Number of cells [1]	30
Concentration of vanadium ions [mol m^{-3}]	1600
Volume of one half-cell [l]	2.16
Volume of one tank [l]	900

Table 3
Values of analogous resistors.

Part of geometry	Electrolyte side	Resistivity [Ω] at SOC 0	Resistivity [Ω] at SOC 1
Channel	Anolyte	1276.19	815.09
Channel	Catholyte	815.09	547.39
Manifold	Anolyte	1.579	1.008
Manifold	Catholyte	1.008	0.677
Pipe	Anolyte	29.10	18.59
Pipe	Catholyte	18.59	12.48
Tube	Anolyte	4.37	2.79
Tube	Catholyte	2.79	1.87

charge time and the shorter discharge time lead to a small displacement of the curve. In total, however, the complete charge/discharge cycle have nearly the same duration in all three cases.

4.3.1. Effects on the setup with inlets and outlets on the same side

For a single stack, the shunt current exhibits a maximum in the manifolds of the cells in the middle of the stack. This is shown in Fig. 7 in the model validation section. In Fig. 9, the shunt currents in the manifolds of the 15th cell of the stacks with 30 cells are presented. In Fig. 7, the shunt current in all manifolds at one state-of-charge is shown whereas in Fig. 9 the shunt currents in one manifold are shown for different conditions of state-of-charge, charge and discharge regime over time. Because of the different setups there are two subfigures, for the setup with inlets and outlets a) on the same side and b) on opposing sides of the stack. The black graphs are calculated for the setup without any connections. In this case, the shunt currents in each stack and their graphs are identical, so only one line is shown.

The dependence of the ionic conductivities on the state-of-charge yields a significant change of the occurring shunt currents, as shown in Fig. 9a). The shunt currents increase with rising state-of-charge; the shunt currents in this cell at a state-of-charge of 0.95 are about double the shunt currents at a state-of-charge of 0.05. More important, the shunt currents within a stack change due to the external connection. They become markedly different in the three stacks. In stack 2, the shunt current in the 15th cell of the same side setup is nearly the same as the one of the no connections setup. The same comparison yields a threefold increase for the same side setup in stack 1. The shunt current of this cell has about
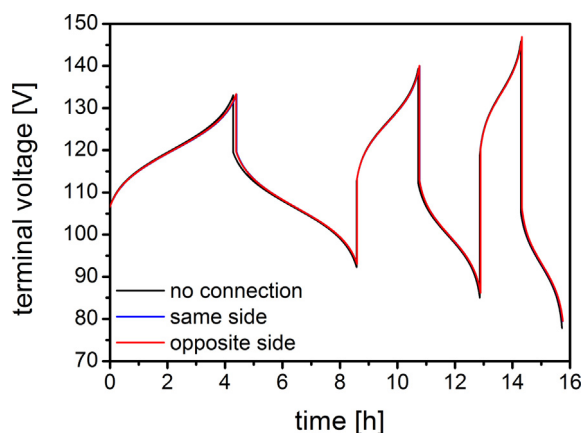

Fig. 8. Three charge/discharge cycles at current densities of 25, 50 and 75 mA cm^{-2} for three redox flow battery stacks which are electrically connected in series. Comparison of the calculated terminal voltages with black: no pipe connection between stacks, blue: inlet and outlet are on the same side of the stacks, red: inlet and outlet are on opposite sides of the stacks. (For interpretation of the references to colour in this figure legend, the reader is referred to the web version of this article.)

the same value in stack 3 but its direction is inverted. The catholyte shunt currents exhibit the same pattern but their peaks are about 0.8 A for the first stack and −0.3 A for the third stack, which is about 160% and 150% of the values for the anolyte shunt currents.

Fig. 10 is constructed analogous to Fig. 7 in order to illustrate the shunt currents in the anolyte manifolds and channels of all cells. The subfigures a) through c) represent the manifolds and channels of the electrolyte feed, "lower part", of the three stacks and d) through f) the manifolds and channels of the electrolyte removal, called "upper part". To account for the state-of-charge dependency, three shunt currents are depicted for a state-of-charge of 0.1, 0.5 and 0.9. The shunt currents in the channels flow between the manifold and the cells, so the subfigures a)–d), b)–e) and c)–f) are connected by the cells in-between. Only one setup is presented in this way in order to avoid several figures that look similar. Whereas patterns similar to those in subfigures a)–c) are present in all stack setups, the patterns in subfigures d)–f) are only exhibited by the setup with inlets and outlets on opposing sides. The values for the first and the last cells of each stack for the two setups are presented in Table 4.

For the manifolds, a positive sign indicates a shunt current in the direction from cell 30 to cell 1 or "towards the left" in the figures. Conversely, a negative sign indicates a shunt current in the direction from cell 1 to 30 or "towards the right" in the figures. The current in the channels equals the change between cell and shunt currents. Regarding subfigures a)–c), the shunt currents of all manifolds of one stack share the same sign, i.e. they flow in the same direction.

Regarding the setup with inlets and outlets on the same side, stacks 1 and 3 exhibit a different distribution of the shunt currents than the stacks without outer ionic connection. This outer connection yields pronounced shunt currents between these stacks. The highest electric potential is located at the 30th, i.e. last cell of the third stack and the lowest electric potential at the first cell of the first stack. Within each stack, the electric potential increases from cell 1 to 30. Therefore, there are internal shunt currents in the direction of cell 1 and external shunt currents in the direction of stack 1. For the first and the third stack, the larger difference in cell potentials yield external shunt currents that are ten times larger than the internal ones. The external shunt currents override the internal ones, which is depicted in the subfigures a) and c) of Fig. 10. In the first stack, the internal and external shunt currents have opposing directions, whereas these have the same direction in the third stack. Therefore, the sum total of the shunt currents in the first cell of the third stack is slightly higher than in the first cell of the first stack. In both stack 1 and 3, the local maximum of the total shunt currents has shifted from the middle of the stack to the first cell where they are connected to the outer piping.

In stack 2, the shunt current exhibits a similar distribution as in a stack without outer ionic connections. This is because of the odd number of stacks with the same properties which yields minimal external shunt currents for this stack.

Only the anolyte shunt current is shown in the figure. The catholyte shunt currents exhibit the same characteristics, albeit with higher values for the shunt currents. Regarding the values in Table 4, the catholyte shunt currents are about 150% of the anolyte ones.

In Fig. 11, the anolyte and catholyte shunt currents in the outlet tubes are compared. In this setup, the shunt currents in the inlet tubes are identical. This is in agreement with the symmetrical nature of the model setup. Due to the higher conductivity, the shunt currents are higher for the catholyte side. The tube connects the stack to the outer pipes; the shunt current passing this part is the one entering or leaving this particular stack. The external shunt currents flow from stack 1 to stack 3, bypassing stack 2.
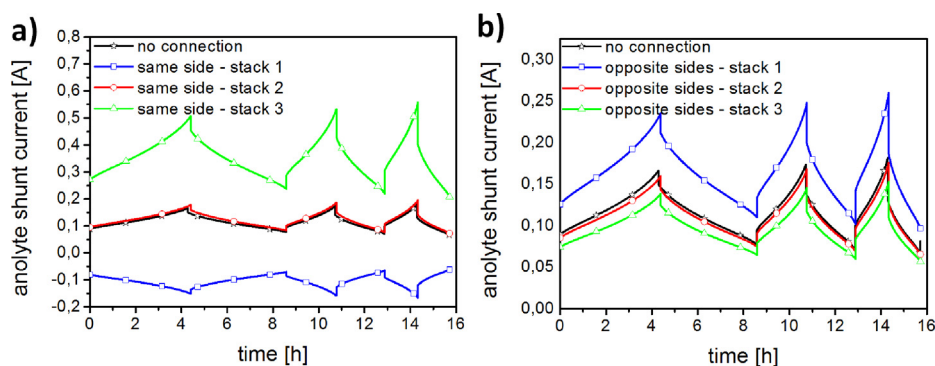
Fig. 9. Three charge/discharge cycles at current densities of 25, 50 and 75 mA cm^{-2} for three redox flow battery stacks which are electrically connected in series with inlets and outlets on a) the same side and b) opposite sides of the stack. Comparison of the calculated anolyte shunt currents occurring in the removal manifold of the 15th cell, i.e. the middle of the three stacks. The black line represents the shunt current without a pipe connection between the stacks.

Comparing the charge and discharge regime of the battery setup, the values of the shunt currents change but the directions and general characteristics remain the same. This is probably because of the same distribution of terminal voltages over the stacks.

4.3.2. Effects on the setup with inlets and outlets on opposing sides

In this test case, the inlet tubes are connected to the lower feed manifold of the first cell of each stack and the outlet tubes are connected to the upper removal manifold of the 30th, i.e. the last
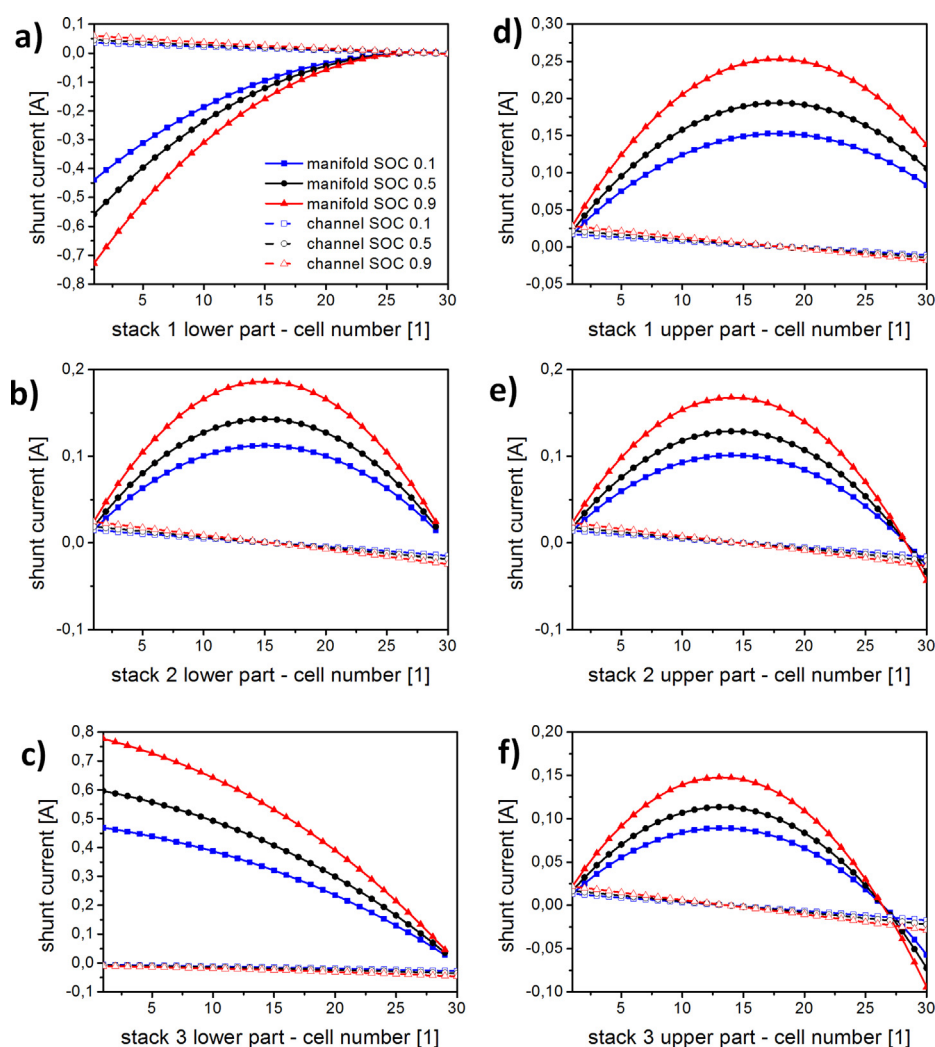

Fig. 10. Distribution of anolyte shunt currents in the manifolds and channels of the three stacks for the electrolyte feed (a–c) and electrolyte removal (d–f) at a charge current density of 75 mA cm^{-2} and a state-of-charge of 0.1, 0.5 and 0.9. The legends in subfigure a) holds for all subfigures. Subfigures d) through f) present the values for the opposite sides setup.

Table 4
Calculated Coulombic (CE) and energy (EE) efficiency ratings for the different setups.

Current density i [mA cm^{-2}]	No connection		Same side		Opposite sides	
	CE [%]	EE [%]	CE [%]	EE [%]	CE [%]	EE [%]
25	99.1	88.7	95.3	84.0	95.9	85.1
50	99.6	79.5	97.6	75.7	98.0	77.9
75	99.7	69.2	98.4	68.6	98.5	68.9

cell of each stack. The resulting shunt currents are different from the same side setup. Especially, different patterns arise in the feed and removal manifolds and channels.

The calculated numbers for the shunt currents in the feed manifold of the 15th cell differ only by a few mA from the numbers of the shunt currents for the same manifold of the same side setup. These changes would not be discernible in a new figure, so it is omitted. The similarity of the shunt currents in the respective feed manifolds in the middle of the stacks is remarkable because in the model, there is a direct electrical connection between the feed and removal channels, shown in Figs. 2, 4 and 5. The high resistances of the channel structures seem to serve as an effective barrier for the shunt currents that follow the electrolyte flows entering and leaving the individual cells.

The pattern of the catholyte shunt currents in the feed manifold of the 15th cell, i.e. the middle of the stacks, are nearly identical to the ones shown in Fig. 9a), albeit with the reported higher values. Within the removal manifold there are the same values, but the signs of the shunt currents of stack 1 and 3 are interchanged. This results from the different setup. For the anolyte side, there are different patterns for the feed and the removal manifold. The feed manifold exhibits the same pattern as the same side setup with similar values. In contrast to the feed manifold, the anolyte shunt currents in this manifold all exhibit the same sign and are significantly lower, shown in Fig. 9b). This indicates a different distribution of anolyte shunt currents within the removal manifold which is presented in Fig. 10d) through f). Because the outer ionic connection is on the opposite side of the stack for the manifolds and channels of the removal flow, it could be expected that the shunt currents are simply reversed. This is nearly true for the shunt currents of the catholyte side.

The shunt currents of the anolyte side, presented in Fig. 10d)–f) exhibit a different pattern. Firstly, the total values of the shunt currents within the removal manifolds is less than the values within the feed manifolds. Secondly, the shunt currents in Fig. 10e) and f) display different directions within a stack. In subfigure e), the shunt currents are positive in the cells 1–27, indicating a flow towards cell 1. In the remaining cells 28–30, the shunt currents have a negative sign, i.e. their flow direction is toward cell 30 and out of

the stack. The same pattern holds for the manifolds of the removal feed of stack 3 in subfigure f): the shunt currents in cells 1–26 have a positive sign whereas they have a negative sign in cells 27–30. For the anolyte side, the external shunt currents that cross the outlet tubes are lower than the ones in the inlet tubes. This indicates that the pathway through the cells of the stacks is preferred above the pathway through the outlet tubes. There is no preferred pathway for the shunt currents of the catholyte side. This seems to be caused by the lower conductivity of the anolyte solution. If the conductivity of the anolyte solution is set to the conductivity of the catholyte solution, the preference for one pathway disappears. The conductivity of the electrolyte solutions therefore influences the distribution pattern of the shunt currents (Fig. 12).

4.3.3. Efficiencies of the different setups

Energy storage systems can be rated by their efficiencies. The Coulombic efficiency CE compares the total amount of electric charge during charge and discharge operation

$$CE = \int I \, dt^{\text{discharge}} \Big/ \int I \, dt^{\text{charge}}, \tag{16}$$

and the energy efficiency EE the total energy converted during charge and discharge

$$EE = \int EI \, dt^{\text{discharge}} \Big/ \int EI \, dt^{\text{charge}}. \tag{17}$$

The calculated Coulombic and energy efficiencies for the three stack setups and different current densities are presented in Table 4. In the first column, there is the Coulombic efficiency for three stacks without a connection between them. There are only internal shunt currents present in this case. These are rather small, less than 0.9% of the total charge.

The introduction of pipe connections between the three stacks decreases both the Coulombic and the energy efficiency of the whole battery system. This decrease is slightly larger for the setup with inlets and outlets on the same side of the stack. For a current density of 25 mA cm^{-2}, the loss in Coulombic efficiency for these setups amounts to about 5%, which is a five-fold increase on the loss in the setup without any connections. This is due to the additional external shunt currents and the increase of the internal shunt currents. With an increase of the applied current density, the Coulombic efficiency also increases whereas the energy efficiency decreases. For higher current densities, the time of the charge and the discharge operation is reduced, which in turn yields lower total losses by shunt currents. The needed voltage for charge operation is
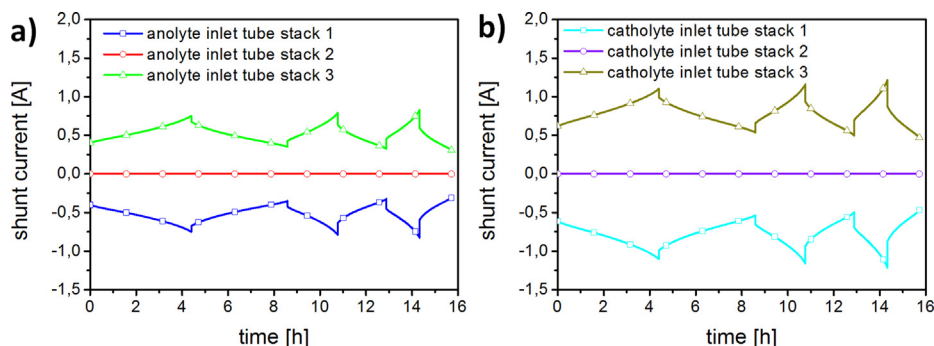

Fig. 11. Shunt currents in the a) anolyte and b) catholyte outlet tubes with inlets and outlets at the same side of the stacks.
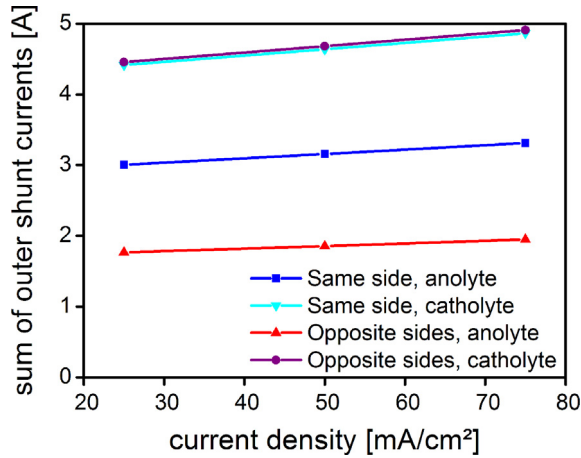
Fig. 12. Shunt currents in the a) anolyte and b) catholyte outlet tubes with inlets and outlets on opposing sides of the stacks.

increased and for discharge operation decreased, lowering the energy efficiency. The differences in the efficiencies between the different stack setups decrease with higher current densities. This is also illustrated in Fig. 13, in which the differences between the outer charge or discharge current and the current passing through the cells of the stacks are shown. The current difference I_{diff} is defined as

$$I_{diff} = \frac{\sum^{stacks}\sum^{cells}I_{cell}}{n_{stacks}\,n_{cells}} - I_{charge/discharge}, \quad (18)$$

with the sum of all currents passing through the cells I_{cell} of every stack. These currents partake in the electrochemical energy conversion. I_{charge} and $I_{discharge}$ are the charge and discharge currents applied by the external current source. Charge currents have a positive, discharge currents a negative sign. The current difference equals the sum of all internal and external shunt currents and is calculated for three charge and discharge cycles of 25, 50 and 75 mA cm^{-2}. The corresponding terminal voltages of the whole battery system are shown in Fig. 8. Although the applied current density is doubled and tripled in the second and third cycle, the total sum of the induced shunt currents increases slightly for the charge operation and decreases slightly for the discharge operation.
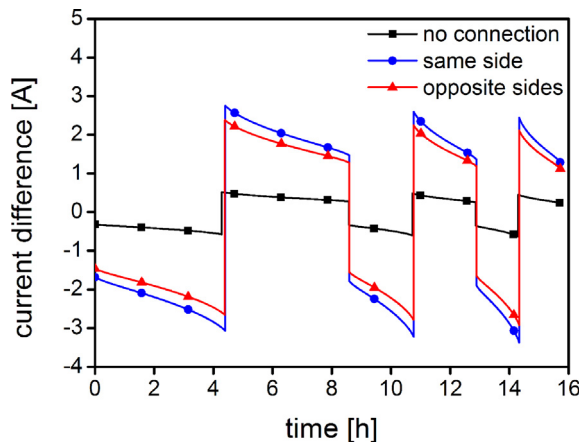

Fig. 13. Sum total of all shunt currents as difference between the current set by the outer current source and the current passing through the cells for three charge and discharge cycles of 25, 50 and 75 mA cm^{-2}.

This holds with the terminal voltages shown in Fig. 8, which show minor increases or decreases for the later charge and discharge operations.

5. Summary and future development

A model for the shunt currents in all-vanadium redox flow battery consisting of three stacks which are electrically connected in series has been developed. The model uses an equivalent circuit to represent the ionic connections between the cells and the stacks which make up the pathways of the shunt currents. The model considers the dependence of the electrolyte conductivities at different state-of-charges, which have been measured. It has been validated using a single stack and static properties for the equivalent circuit and comparing the calculated results with published data.

The model has been used to simulate three galvanostatic charge/discharge cycles at different currents. The introduction of state-of-charge dependent ionic conductivities for the electrolyte solutions yields twice the shunt currents at a state-of-charge of 0.95 compared to the shunt currents at a state-of-charge of 0.05. The model battery consists of three stacks, which are simulated for different pipe network setups. These are no pipe connection between the stacks, inlet and outlet pipes on the same side of the stacks and inlet and outlet pipes on opposite sides of the stacks. The pipe connections add external shunt currents to the system and they also increase the internal shunt currents within the stacks. This yields an increase in the loss of Coulombic efficiency from 0.5% for the three stacks without pipe connections to 2.5%. Prokopius [11] asserts that the shunt power loss of a redox flow battery stack increases exponentially with the number of cells in a stack. Future work could explore whether this also holds for larger arrays of stacks. This would have a large impact on the economic feasibility of large-scale redox flow batteries.

The simulated results show that the shunt currents for the setups with pipe connections are not distributed equally. This could lead to corrosion at places that are subject to higher shunt currents.

The model can be used to investigate different parameters of the battery system. The effect of the shunt currents on the Coulombic efficiency increases over time, so different tank sizes can be evaluated for a battery system. Longer pipes are a common solution to the external shunt currents. However, this leads to additional pressure losses, which increase the needed pumping power. Protective currents have been proposed [29] to reduce the amount of shunt currents. An expanded model could evaluate the effectiveness of such a measure.

Another consideration for future work could be the addition of activation potentials to the cell model. The model of this work considers only Ohmic resistances and a Nernst equation based on concentrations. It could therefore underestimate the actual shunt currents.

Acknowledgments

List of symbols

Latin

A	diameter within a part of the piping [m^2]
c	concentration [mol/m^3]

CAPE	computer aided process engineering
CE	Coulombic efficiency [1]
E	equilibrium potential [V]
E	voltage [V]
EE	energy efficiency [1]
$\mathbf{F}$	Faraday constant 96485 [A s mol^{-1}]
$\vec{I}$	current [A]
$\vec{i}$	current density [A/m^2]
l	length within a part of the piping [m]
n	number [1]
n	number of moles [mol]
p	pressure [Pa]
R	resistance [Ω]
$\mathbf{R}$	universal gas constant 8.314[J mol^{-1} K^{-1}]
S	time-dependent state-of-charge [1]
SOC	state-of-charge [1]
T	temperature [K]
t	time [s]
V	volume [m^3]
z	valence [1]

Greek

α	transfer coefficient [1]
λ	ionic conductivity [S m^{-1}]
σ	specific ionic conductivity [S m^{-1}]

Subscripts

a	anolyte
c	catholyte
c	channel
cell	single cell in a stack
diff	difference
e	end of discharge cycle
i	regarding one species
in	i inlet
m	manifold
out	o outlet
p	pipe
s	start of discharge cycle
t	tank quantity/property
t	tube
tot	sum total

Superscripts

eff	effective
ref	reference value
0	standard quantity/property
00	standard property in Nernst equation

References

[1] A.Z. Weber, M.M. Mench, J.P. Meyers, P.N. Ross, J.T. Gostick, Q. Liu, J. Appl. Electrochem. 41 (10) (2011) 1137–1164, http://dx.doi.org/10.1007/s10800-011-0348-2. URL: http://link.springer.com/article/10.1007/s10800-011-0348-2.

[2] N.H. Hagedorn, L.H. Thaller, Design Flexibility of Redox Flow Systems, 17. Intersociety Energy Conversion Engineering conference, Los Angeles, CA, USA, 8 Aug 1982, p. 1982.

[3] C. Ponce de León, A. Frias-Ferrer, J. González-García, D. Szánto, F.C. Walsh, J. Power Sources 160 (1) (2006) 716–732, http://dx.doi.org/10.1016/j.jpowsour.2006.02.095. URL: http://www.sciencedirect.com/science/article/pii/S037877530600437X.

[4] L. Joerissen, J. Garche, C. Fabjan, G. Tomazic, J. Power Sources. ISSN: 0378-7753 127 (1–2) (2004) 98–104, http://dx.doi.org/10.1016/j.jpowsour.2003.09.066.

[5] F. Díaz-González, A. Sumper, O. Gomis-Bellmunt, R. Villafáfila-Robles, Renew. Sustain. Energy Rev. 16 (4) (2012) 2154–2171, http://dx.doi.org/10.1016/j.rser.2012.01.029. URL: http://www.sciencedirect.com/science/article/pii/S1364032112000305.

[6] A. Poullikkas, Renew. Sustain. Energy Rev. 27 (2013) 778–788, http://dx.doi.org/10.1016/j.rser.2013.07.017. URL: http://www.sciencedirect.com/science/article/pii/S1364032113004620.

[7] M. Skyllas-Kazacos, M. Rychcik, R.G. Robins, A. Fane, M. Green, J. Electrochem. Soc. 133 (1986) 1057–1058.

[8] R.E. White, C. Walton, H. Burney, R. Beaver, J. Electrochem. Soc. 133 (3) (1986) 485–492, http://dx.doi.org/10.1149/1.2108606. URL: http://jes.ecsdl.org/content/133/3/485.short.

[9] H. Burney, R.E. White, J. Electrochem. Soc. 135 (7) (1988) 1609–1612, http://dx.doi.org/10.1149/1.2096069. URL: http://jes.ecsdl.org/content/135/7/1609.short.

[10] J.A. Schaeffer, L.-D. Chen, J.P. Seaba, J. Power Sources 182 (2) (2008) 599–602, http://dx.doi.org/10.1016/j.jpowsour.2008.04.014. URL: http://www.sciencedirect.com/science/article/pii/S0378775308007234.

[11] P.R. Prokopius, Model for Calculating Electrolytic Shunt Path Losses in Large Electrochemical Energy Conversion Systems, NASA STI/Recon Technical Report N 76 (1976) 21702, URL: http://adsabs.harvard.edu/abs/1976STIN...7621702P.

[12] N. Hagedorn, M.A. Hoberecht, L.H. Thaller, NASA-Redox Cell-stack Shunt Current, Pumping Power, and Cell-performance Tradeoffs, Tech. Rep., National Aeronautics and Space Administration, Cleveland, OH (USA), 1982. Lewis Research Center

[13] D. Stalnaker, A. Lieberman, Design and assembly considerations for Redox cells and stacks, NASA Technical Memorandum, NTIS Accession Number DE82000415, 1981.

[14] R.S. Jupudi, G. Zappi, R. Bourgeois, J. Appl. Electrochem. 37 (8) (2007) 921–931, http://dx.doi.org/10.1007/s10800-007-9330-4. URL: http://link.springer.com/article/10.1007/s10800-007-9330-4.

[15] G. Codina, A. Aldaz, J. Appl. Electrochem. 22 (7) (1992) 668–674, http://dx.doi.org/10.1007/BF01092617. URL: http://link.springer.com/article/10.1007/BF01092617.

[16] G. Codina, J. Perez, M. Lopez-Atalaya, J. Vasquez, A. Aldaz, J. Power Sources. ISSN: 0378-7753 48 (3) (1994) 293–302, http://dx.doi.org/10.1016/0378-7753(94)80026-X. URL: http://www.sciencedirect.com/science/article/pii/037877539480026X.

[17] E. Henquín, J. Bisang, J. Appl. Electrochem. 37 (8) (2007) 877–886, http://dx.doi.org/10.1007/s10800-007-9324-2. URL: http://link.springer.com/article/10.1007/s10800-007-9324-2.

[18] E. Henquín, J. Bisang, J. Appl. Electrochem. 38 (9) (2008) 1259–1267, http://dx.doi.org/10.1007/s10800-008-9550-2. URL: http://link.springer.com/article/10.1007/s10800-008-9550-2.

[19] E. Henquín, J. Bisang, J. Appl. Electrochem. 39 (10) (2009) 1755–1762, http://dx.doi.org/10.1007/s10800-009-9874-6. URL: http://link.springer.com/article/10.1007/s10800-009-9874-6.

[20] F. Xing, H. Zhang, X. Ma, J. Power Sources 196 (24) (2011) 10753–10757, http://dx.doi.org/10.1016/j.jpowsour.2011.08.033. URL: http://www.sciencedirect.com/science/article/pii/S0378775311015333.

[21] A. Tang, J. McCann, J. Bao, M. Skyllas-Kazacos, Investigation of the effect of shunt current on battery efficiency and stack temperature in vanadium redox flow battery, J. Power Sources (2013), http://dx.doi.org/10.1016/j.jpowsour.2013.05.079. URL: http://www.sciencedirect.com/science/article/pii/S0378775313008690.

[22] A. Tang, J. Bao, M. Skyllas-Kazacos, J. Power Sources 196 (24) (2011) 10737–10747, http://dx.doi.org/10.1016/j.jpowsour.2011.09.003. URL: http://www.sciencedirect.com/science/article/pii/S0378775311017095.

[23] S. König, M. Zimmerlin, T. Leibfried, F.T. Wandschneider, S. Röhm, P. Fischer, in: ETG-Kongress 2013: Energieversorgung auf dem Weg nach 2050, 5th–6th November 2013, VDE, Berlin, Germany, 2013.

[24] C.J. Barnhart, M. Dale, A.R. Brandt, S.M. Benson, Energy Environ. Sci. 6 (2013) 2804–2810.

[25] A. Tang, J. Bao, M. Skyllas-Kazacos, J. Power Sources 248 (2014) 154–162, http://dx.doi.org/10.1016/j.jpowsour.2013.09.071. URL: http://www.sciencedirect.com/science/article/pii/S037877531301567X.

[26] D. You, H. Zhang, J. Chen, Electrochim. Acta 54 (27) (2009) 6827–6836, http://dx.doi.org/10.1016/j.electacta.2009.06.086. URL: http://www.sciencedirect.com/science/article/pii/S0013468609009128.

[27] M. Skyllas-Kazacos, M. Kazacos, J. Power Sources 196 (20) (2011) 8822–8827, http://dx.doi.org/10.1016/j.jpowsour.2011.06.080. URL: http://www.sciencedirect.com/science/article/pii/S0378775311013176.

[28] T. Mohammadi, M. Skyllas-Kazacos, J. Power Sources 56 (1) (1995) 91–96. URL: http://www.sciencedirect.com/science/article/pii/0378775395800148.

[29] M. Zahn, P.G. Grimes, R.J. Bellows, Shunt Current Elimination and Device, US Patent 4,197,169, 1980.

URL: http://www.sciencedirect.com/science/article/pii/S0378775303009431. eighth Ulmer Electrochemische Tage.